



*Citation for published version:*

Muddle, DM & Briggs, KM 2019, 'Macropore structure and permeability of clay fill samples from a historic clay fill earthwork', *Transportation Geotechnics*, vol. 19, pp. 96-109. <https://doi.org/10.1016/j.trgeo.2019.02.003>

*DOI:*

[10.1016/j.trgeo.2019.02.003](https://doi.org/10.1016/j.trgeo.2019.02.003)

*Publication date:*

2019

*Document Version*

Peer reviewed version

[Link to publication](#)

*Publisher Rights*

CC BY-NC-ND

**University of Bath**

**Alternative formats**

If you require this document in an alternative format, please contact:  
[openaccess@bath.ac.uk](mailto:openaccess@bath.ac.uk)

**General rights**

Copyright and moral rights for the publications made accessible in the public portal are retained by the authors and/or other copyright owners and it is a condition of accessing publications that users recognise and abide by the legal requirements associated with these rights.

**Take down policy**

If you believe that this document breaches copyright please contact us providing details, and we will remove access to the work immediately and investigate your claim.

1 **Title:** Macropore structure and permeability of clay fill samples from a historic clay fill earthwork

2

3 **Authors:** D. M. Muddle<sup>1</sup> & K.M. Briggs<sup>1\*</sup>

4 <sup>1</sup>Department of Architecture & Civil Engineering, University of Bath, Bath, UK. BA2 7AY.

5 \*Corresponding author

6

7 **Words:** 4391 (main text)

8 **Tables:** 6

9 **Figures:** 13

10

11 **Abstract:**

12 Near surface macropores and macro features (e.g. cracks and fissures) provide pathways for rapid  
13 water infiltration into the core of clay fill earthworks. However it is more difficult to measure the size  
14 and distribution of macropores located below the weathered soil surface (>1.5 m depth) and hence  
15 assess their influence on water flow through the clay fill core of an earthwork.

16 This paper explores the influence of macropores on the rate of water flow within the core of a  
17 historic railway earthwork. Samples were excavated from the core (1.5 m – 6.5 m depth) of a clay fill  
18 railway embankment and subjected to laboratory saturated hydraulic conductivity testing. The  
19 samples were scanned using X-ray computed tomography (XCT) before and after laboratory testing.  
20 XCT was used to measure the size and distribution of macropores ( $>63 \times 10^{-6}$  m) within the samples  
21 and compare with the saturated hydraulic conductivity measurements.

22 The results showed that the distribution of macropores and the saturated hydraulic conductivity of  
23 the samples from the embankment core was not dependant on the depth of excavation. The total  
24 macroporosity of the samples was very small relative to the total porosity (less than 10%). The  
25 saturated hydraulic conductivity of the samples was more closely related to the connectivity of the  
26 macropores (mean length) than to the total porosity or the total macroporosity.

27 The macropores were variably distributed within the core of the clay fill embankment, they did not  
28 show a clear relationship with depth and they were connected over relatively short lengths (the  
29 mean macropore length was not greater than  $1.6 \times 10^{-3}$  m). Therefore water flow through the core of  
30 the embankment is likely to be through the clay fill matrix, rather than through the connected  
31 macropore pathways which allow rapid water infiltration at the near soil surface (<1.5 m depth).

## 32 1. Introduction

33 Changes in pore water pressure critically influence the strength and volume change of clay fill soils.  
34 This affects the long-term performance (deformation and stability) of earthworks constructed from  
35 these materials (Glendinning *et al.*, 2014; Briggs *et al.*, 2017). Such structures include new and  
36 historic railway and highway embankments, flood embankments and embankment dams.

37 There is evidence that near surface macropores and macro features (e.g. cracks and fissures) provide  
38 pathways for rapid water infiltration into the core of clay fill earthworks (Dyer *et al.*, 2009; Li *et al.*,  
39 2011; Dixon *et al.*, 2018). This can increase the rate of pore water pressure rise within earthworks in  
40 response to environmental changes such as precipitation and flooding events. Macropores can also  
41 act as preferential flow paths in soils below the near surface zone (Beven & Germann, 2013).

42 However, there is limited data showing the size and connectivity of macropores within the core of  
43 clay fill embankments. Therefore, it is difficult to establish whether preferential flow occurs through  
44 connected macropores or through the clay fill matrix; as is assumed in simulations of embankment  
45 hydrology (Kovacevic *et al.*, 2001; Scott *et al.*, 2007; O'Brien, 2013, Briggs *et al.*, 2016).

46 It can be difficult to measure the size and distribution of macropores within soils without disturbing  
47 the sample structure. Recent research (e.g. Perret *et al.*, 1999; Mooney, 2002; Mees and London,  
48 2003; Luo *et al.*, 2008; Anderson *et al.*, 2010; Peth *et al.*, 2010; Mooney *et al.*, 2012; Geistlinger,  
49 2013; Naveed *et al.*, 2013; Shin *et al.*, 2013; Lamorski *et al.*, 2014; Larsbo *et al.*, 2014; Katuwal *et al.*,  
50 2015; Eck *et al.*, 2016) has explored the use of computed tomography to visualise macropore  
51 structure within small (<50 mm) samples of reconstituted soil. However, the technique has not been  
52 used to measure macropores within larger, denser samples of *in situ* clay fill, nor has it been used to  
53 explore the distribution of macropores through the core of an earthwork.

54 This paper presents an investigation into the use of X-ray computed tomography (XCT) to visualise  
55 and measure macropore structure ( $>63 \times 10^{-6}$  m) within 100 mm diameter samples of clay fill. XCT  
56 and laboratory testing is used to explore relationships between the macropore structure and  
57 saturated hydraulic conductivity of clay fill samples obtained from the core (1.5 m to 6.5 m depth) of  
58 a historic railway earthwork.

## 59 2. Method

60 Soil samples were obtained from Laverton Embankment (Figure 1) in Gloucestershire, in south-west  
61 England. The embankment is approximately 6m high and it was built between 1900 and 1906 as part  
62 of the Honeybourne Line, which now forms the Gloucestershire-Warwickshire Steam Railway. Many  
63 railway embankments of this period were constructed by end-tipping locally excavated clay to form  
64 poorly compacted, 'dumped' clay fill embankments (Vaughan *et al.*, 2004; Briggs *et al.*, 2017).

65 Six soil cores (87-102 mm diameter, 160 mm height) were extracted from a borehole at the crest of  
66 Laverton Embankment at approximately 1m intervals between 1.5 m and 6.5 m depth. Intact  
67 samples were obtained from within the core of the earthwork rather than from the more variable  
68 near surface soil (<1.5 m depth), where dynamic weathering processes (e.g. desiccation cracking,  
69 plant roots) and seasonal soil moisture variation would influence the soil structure (Smethurst *et al.*,  
70 2003; Glendinning *et al.*, 2014; Dixon *et al.*, 2018). Boreholes drilled along the length of the  
71 embankment showed that a variable upper layer of fouled ballast (approximately 0.9 m thick)  
72 overlaid clay fill formed from locally excavated, end-tipped Charmouth Mudstone (Gunn *et al.*,  
73 2016). The cores were collected using cable-percussion drilling with a Dando Terrier 2002 rig. This  
74 allowed the recovery of continuous 1 m long samples captured in polyvinyl chloride (PVC) liners. The  
75 diameter of the two deepest cores was reduced from 102 mm to 87 mm during drilling to reduce

76 sampling resistance at these depths. The sample from 6.5 m depth was disturbed during drilling so it  
77 was not possible to determine if this was clay fill or clay from the embankment foundation.

78 While it is difficult to obtain perfectly undisturbed samples for testing (Clayton and Siddique, 2001),  
79 disturbance was minimalised in every part of the sampling process. After trimming, the samples  
80 were stored in PVC tubes with secure end caps to prevent mechanical disturbance and evaporation.  
81 The samples were stored in a refrigerator at 3°C. Table 1 shows the size, sampling depth, bulk  
82 density and gravimetric water content of the samples. A 100 mm diameter, reconstituted sample  
83 was prepared from sample 4C (3.5 m depth) using wet compaction to a bulk density of  $1.91 \times 10^{-3}$   
84  $\text{kg/m}^3$ . Particle size distributions were obtained for the samples from 3.5 m and 4.5 m depth using  
85 wet sieving and hydrometer tests (BS 1377-2:1990). These showed that the samples were well  
86 graded, consisting of 45% clay, 50% silt and 10% sand particles. Soil index testing showed that the  
87 liquid and plastic limits of the samples were between 61-77% and 27-37% respectively. X-Ray  
88 diffraction analysis of the clay fill was undertaken using a Bruker D8 Advance X-ray powder  
89 diffractometer with CuK $\alpha$  radiation. This showed that the clay fraction of the fill ( $< 2 \times 10^{-6}$  m)  
90 consisted of Quartz, Calcite, Kaolinite, Illite and Sodium Magnesium Aluminium Silicate.

91 XCT scans were undertaken at multiple stages in the laboratory testing process. First, the samples  
92 were scanned to obtain macropore information prior to laboratory testing. Second, the samples  
93 were saturated within a triaxial cell and subjected to constant head permeability testing. The  
94 samples were then removed and scanned in the saturated condition. Finally, the triaxial cell samples  
95 were divided into three smaller samples and subjected to one-dimensional consolidation tests. The  
96 details relating to each of these stages is described in more detail below.

## 97 2.1 XCT scanning and analysis procedure

98 X-ray computed tomography is a 3D imaging process that is based on the principle of  
99 electromagnetic wave attenuation. X-rays emitted from the source pass through the sample and are  
100 attenuated by absorption and scattering (Mooney *et al.*, 2012). The degree of attenuation along any  
101 x-ray path is controlled by the materials it passes through (each of which has a linear attenuation  
102 coefficient ( $\mu$ ) dependent on the electron density of the material) and the X-ray energy. The X-rays  
103 are then converted to photons and recorded using a scintillator-fronted detector. As the sample is  
104 rotated, 2D grey-scale images (projections) are collected from many angles. Each image records the  
105 total attenuation of the X-rays. The 2D projection data are then reconstructed into a 3D volume  
106 using numerical algorithms, and can then be visualised as a 3D voxelised volume (a voxel is the 3D  
107 equivalent of a pixel) where the intensity or brightness of each voxel represents the attenuation, and  
108 therefore density of the material in that voxel volume. The size of the voxels reflects the spatial  
109 resolution of the scan.

110 Although visual inspection is a valuable qualitative tool, the image data can be quantified using  
111 software packages such as Avizo (FEI Visualization Sciences Group), CT Analyser (Skyscan-Bruker) or  
112 Fiji (Schindelin *et al.*, 2012). As the greyscale is related to the material composition, the porosity of a  
113 material, or the volume fraction of any phase (e.g. solid, liquid) or mineral can be determined by  
114 counting the number of voxels assigned to it during segmentation of the sample (see Appendix).  
115 Quantitative 3D analysis is made challenging by artefacts within the image data (e.g. image noise,  
116 beam hardening, ring artefacts), poor greyscale contrast between the different phases and minerals  
117 (better contrast is achieved at lower energies but at the cost of poorer transmission and lower signal  
118 to noise), and insufficient spatial resolution (often called the partial voxel effect) which causes a  
119 voxel to be made up of several minerals or phases and causes averaging and blurring of phase  
120 boundaries (Cnudde & Boone, 2013). For these reasons, CT investigations in the geosciences (Pender

121 *et al.*, 2009; Ito & Azam, 2017; Wildenschild & Sheppard, 2013) have generally used smaller sample  
122 sizes (< 50 mm).

123 The samples were scanned using a Nikon X-Trek XTH225ST with a maximum accelerating voltage of  
124 195kV at 105 mA. The beam was pre-filtered using 0.5 mm Cu to reduce beam hardening. A total of  
125 1800 projections were taken over 360-degree rotation with a two-second exposure time. Data were  
126 reconstructed using the Nikon proprietary filtered back projection algorithm, with a voxel resolution  
127 of  $53\text{-}63 \times 10^{-6}\text{m}$  (see Table 3; after Muddle, 2017).

128 The XCT scan settings shown in Table 2 were used to examine the clay fill samples. Initial  
129 investigations (Muddle, 2017) showed that it was not possible to scan a larger (300 mm) block  
130 sample of clay fill without reducing image resolution, losing greyscale contrast between the mineral  
131 phases and forming excessive imaging artefacts such as beam hardening.

132 The image processing and interpretation followed the procedure developed by Muddle (2017), as  
133 outlined in the Appendix. The images were reconstructed using the Nikon proprietary software  
134 (Nikon, 2019). The software contains correction algorithms to reduce ring artefacts, beam hardening  
135 and noise. The same reconstruction settings were used for each sample to aid comparison of the  
136 data and the repeatability of the tests. However the impact of these algorithms on the image  
137 reconstruction were not explored, hence they may not represent the best available method.

138 Four different methods of image enhancement were explored (a median filter, sharpened filter, non-  
139 local means filter and Gaussian filter). The effectiveness of these methods was measured by  
140 comparing the degree of contrast from the image slices and greyscale histograms. A sharpened  
141 median filter was identified as the most effective and computationally efficient image improvement  
142 process (see Appendix). Initial investigations showed that automated watershed thresholding  
143 (Iassonov *et al.*, 2009), was not appropriate for the clay fill samples (see Appendix). Manual  
144 interactive thresholding was required for the clay fill samples because they were dense samples with  
145 intensity histograms that lacked complete definition. A two-voxel partial volume correction was used  
146 for the clay fill samples because it minimally altered the macroporosity measurement (less than  
147 0.04% for the samples tested) but removed a large number of objects from the image. The influence  
148 of the partial volume correction on the measured pore properties is shown in the Appendix.

149 Preliminary investigations (Muddle, 2017) were used to develop a rigorous and repeatable image  
150 analysis method, which allowed the macropore properties of the clay fill samples shown in Table 1  
151 to be compared. Due to the inherent variability of the 100 mm diameter samples, the scans were  
152 performed at a range of voxel sizes. Table 3 shows the voxel resolution achieved from each scan. To  
153 keep the resolution constant between repeated scans of the same sample and to allow for  
154 comparison of the evolution of the macropore structure with saturation, the partial volume effect  
155 correction was matched between corresponding samples. A 40 mm sub volume at the centre of the  
156 sample was used for subsequent image processing and analysis, to reduce computational demand.

157 The consistency of the image analysis procedure was explored by examining the results of the three  
158 scans over the height of sample 5C (at the top, middle, and bottom of the sample). Data from three  
159 individual scans was processed independently; however there was some crossover (overlap) in the  
160 scans. This allowed the scans to be compared, showing that the volume of voids per slice in the  
161 sample aligned almost exactly (Figure 2).

## 162 2.2 Saturated hydraulic conductivity testing

163 Saturated hydraulic conductivity ( $K_{sat}$ ) measurements were undertaken using the samples from  
164 Laverton Embankment. This allowed a direct comparison with the macropore property metrics

165 measured using XCT. However it should be noted that this sample size (102 mm diameter) may limit  
166 the ability to measure the permeable fabric within a clay fill embankment, which requires 250 mm  
167 diameter samples (Rowe, 1972), or *in situ* testing to measure the presence of larger cracks and  
168 fissures within the near surface (<1.5 m depth) soil (Dixon *et al.*, 2018).

169 The samples were installed in the triaxial cell and saturated using backpressure saturation (B-ratio >  
170 95%). The use of CO<sub>2</sub> flushing was explored to achieve higher saturation, but this was ineffective.  
171 The effective stresses applied to the samples replicated field conditions at the depth from which the  
172 samples originated (Table 1). Constant head permeability tests were undertaken according to BS  
173 1377-5:1990 (British Standards Institution, 1990) using a hydraulic gradient (*i*) of 125. The  
174 saturated hydraulic conductivity was calculated using Darcy's Law (Darcy, 1856).

175 The triaxial samples were divided into three layers and subjected to three, one-dimensional  
176 oedometer consolidation tests according to BS 1377-5:1990. The saturated hydraulic conductivity of  
177 the samples was calculated using Terzaghi's (1943) consolidation theory.

### 178 2.3 Mercury intrusion porosimetry (MiP) testing

179 Mercury intrusion porosimetry (MiP) testing was undertaken using the reconstituted sample and  
180 sample 5C<sub>(bot)</sub> from 4.58 m depth. This was used to measure pores in the samples which were not  
181 captured by the XCT technique. MiP involves applying an absolute pressure to mercury (a non-  
182 wetting fluid) in order to force it to enter pores within the sample. If the pores are assumed to be of  
183 cylindrical shape then the pore diameter can be estimated using the Washburn equation (Washburn,  
184 1921). The surface tension of mercury was taken to be equal to 0.484 N/m at 25°C (Smith, 2015).  
185 The contact angle between mercury and the pore wall is usually taken between 139° and 147° for  
186 clays (Diamond, 1970), so 140° was used in these tests.

187 Mercury intrusion porosimetry can be used to estimate porosity for pore diameters between  $4 \times 10^{-9}$   
188 m and  $0.4 \times 10^{-3}$  m. This is a much finer resolution than is possible using XCT (greater than  $50 \times 10^{-6}$   
189 m). However, MiP does have several limitations when applied to this investigation. First, it is not  
190 possible to measure isolated pores that are completely enclosed by solids and it is not possible to  
191 measure pores that are only accessible through smaller ones. Second, the minimum practical  
192 pressure of the machine limits the largest size of pore that can be measured. Mostly critically, MiP  
193 requires the use of very small samples (less than 0.001kg) which must be oven dried or freeze-dried  
194 prior to testing. This limits the usefulness of MiP when investigating the influence of macropores on  
195 the saturated hydraulic conductivity of the clay fill samples (i.e. the pores with a diameter  $>0.4 \times 10^{-3}$   
196 m). However, it does give an indication of the volume of pores that were not captured by the XCT  
197 images, as a useful comparison. Oven drying of the samples and phase relationships (Powrie, 2014)  
198 were used to obtain the total porosity of the samples over the full range of pore diameter sizes.

### 199 2.4 Method to compare the strength of association between the XCT results and the 200 results of conventional laboratory testing

201 The correlation between the XCT derived property metrics and the laboratory measurements of  
202 sample porosity (*n*), density (*ρ*), and saturated hydraulic conductivity (*K<sub>sat</sub>*), were examined using  
203 Spearman's (1904) correlation coefficient (*r<sub>s</sub>*);  
204

$$205 \quad r_s = 1 - \frac{6 \sum D^2}{N^3 - N}$$

206

207 Where,  $D$  is the difference between the two ranks of each observation and  $N$  is the number of  
208 observations. Spearman's correlation coefficient is a non-parametric test used to measure the  
209 strength of association between two variables, where  $r_s = 1$  means a perfect positive correlation and  
210 the  $r_s = -1$  means a perfect negative correlation.

### 211 3. Results

212 The total macroporosity within the samples (after Partial Volume Effect correction, see Table 4)  
213 ranged from 0.12 % to 4.12 % and the mean macropore length varied between  $0.80 \times 10^{-3}$  m and  $1.6$   
214  $\times 10^{-3}$  m (excluding sample 7C). These values are similar in magnitude to those derived from CT scans  
215 of soils reported in the literature (Luo *et al.*, 2010 (silt loam samples); Naveed *et al.*, 2013 (clay and  
216 sandy clay samples); Shin *et al.*, 2013 (artificial clay samples); Larsbo *et al.*, 2014 (clay loam  
217 samples)).

218 The macropore structure within each of the samples (2C to 7C) was variable (Figure 3). Some  
219 samples contained large, isolated macropores (Figure 3a), some contained biological-type pores  
220 running through the sub volume (Figure 3b) and the reconstituted sample (Figure 3c) contained a  
221 more uniform size and spatial distribution of macropores. A comparison of the volume of voids per  
222 slice in each of the samples shows that there is no clear variation in the distribution of macropores  
223 with depth within the embankment core (Figure 4). This was also evident in the three dimensional  
224 macropore visualisations (e.g. as shown in Figure 3). These visualisations showed that Sample 7C was  
225 heavily fractured because of disturbance during excavation. This is evidenced by the large range of  
226 the volume of voids in Sample 7C (Figure 4).

227 The laboratory saturation procedure reduced the total macroporosity, the macropore density and  
228 the macropore surface area density within the samples (Table 4). Some consolidation may have  
229 occurred due to the high hydraulic gradient used for the test, or when the pore pressure within the  
230 samples was lowered (relative to the cell pressure) before they were removed from the triaxial cell  
231 (Pender *et al.*, 2009). Figure 5 shows the pore size distribution per slice (as a percentage of total  
232 pore volume) through the 40 mm cubed sub volumes in samples 2C, 3C and 4C. This shows that the  
233 saturation procedure decreased the volume of pores per slice and increased the macropore  
234 uniformity of the samples. The saturation procedure also reduced the size of the largest macropores  
235 within each sample, indicating that these pores are more likely to be affected by the saturation  
236 procedure than the smaller pores within the samples. This is in agreement with evidence showing  
237 that larger pores close first during the compaction of sediments (Delage & Lefebvre, 1984).

238 The results of the MiP tests for Sample 5C<sub>(bot)</sub> and the Reconstituted Sample are shown in Table 5.  
239 The porosity measured using the MiP technique was significantly lower than that measured using  
240 phase relationships (e.g. 26% and 50% respectively for the Reconstituted Sample). The MiP data  
241 showed that the samples contained a modal pore diameter of  $0.05 \times 10^{-6}$  m. This is one thousand  
242 times smaller than can be observed using the XCT images. Both the MiP and the total porosity values  
243 are much larger than the porosity of the samples measured using XCT. This shows that the most  
244 significant proportion of the total porosity consists of pores that are smaller than the macropores  
245 ( $>63 \times 10^{-6}$  m). However, the fewer, larger pores may still influence water flow. Experimental  
246 evidence suggests that pores larger than  $0.3 \times 10^{-3}$  m in equivalent cylindrical diameter are the main  
247 pathways for rapid, non-equilibrium flow (Jarvis, 2007). This indicates that the XCT pore property  
248 metrics will be more representative of these larger pores than the pore sizes measured using total  
249 porosity or MiP.

250 The saturated hydraulic conductivity ( $K_{sat}$ ) measurements from triaxial permeability tests and one-  
251 dimensional consolidation tests are compared in Table 6. The  $K_{sat}$  measured using the triaxial  
252 samples was consistently lower than that measured using the oedometer samples. The values of  $K_{sat}$   
253 are comparable with laboratory measurements of London Clay fill reported by O'Brien, *et al.* (2004),  
254 which showed a median  $K_{sat}$  of  $8 \times 10^{-10} \text{ ms}^{-1}$  (range  $3 \times 10^{-9}$  to  $2 \times 10^{-11} \text{ ms}^{-1}$ ) from 34 laboratory tests.  
255 Both the laboratory  $K_{sat}$  values shown in Table 6 and those reported by O'Brien *et al.* (2004) are  
256 approximately two orders of magnitude lower than those measured for clay fill using *in situ* testing  
257 methods (O'Brien *et al.*, 2004; Dixon *et al.*, 2018).

258 Figure 6 shows the Spearman's correlation coefficients for the XCT derived macropore property  
259 metrics and the laboratory measurements of sample porosity, density and saturated hydraulic  
260 conductivity (at the triaxial scale and the oedometer scale). This shows that the total (phase  
261 relationship) porosity has a negative correlation to both the triaxial and the oedometer  
262 measurements of saturated hydraulic conductivity. There is a mild ( $r_s = 0.39$ ) correlation between  
263 the triaxial  $K_{sat}$  and the total macroporosity derived from the XCT data. A closer ( $r_s = 0.71$ ) correlation  
264 is shown between the total macroporosity and the oedometer  $K_{sat}$ . The XCT measured mean  
265 macropore length shows a strong positive correlation with the  $K_{sat}$  measured using both the triaxial  
266 cell ( $r_s = 0.96$ ) and the oedometer ( $r_s = 0.86$ ). This shows that the saturated hydraulic conductivity of  
267 the samples was influenced by the length of the macropores, rather than the quantity of macropores  
268 (total macroporosity).

269 Reference to Table 4 and Table 6 shows that the samples with the greatest mean macropore length  
270 had the highest saturated hydraulic conductivity. The mean macropore length represents a measure  
271 of the connectivity of macropores within the samples. This shows that the connected macropores  
272 were small (mean macropore length up to  $1.6 \times 10^{-3} \text{ m}$ ) but sufficient to provide preferential flow  
273 pathways through the samples. Experimental evidence (Jarvis, 2007) and conceptual models (Jarvis  
274 *et al.*, 2016; Jang *et al.*, 2011) show that this occurs in soils which contain large continuous  
275 macropores but lack well-connected networks of smaller macropores.

276 There is a closer correlation between the pore property metrics and the oedometer  $K_{sat}$   
277 measurements than with the triaxial  $K_{sat}$  measurements. Figure 6 shows a close correlation between  
278 the  $K_{sat}$  measured using the oedometer and all of the pore property metrics. This is because the XCT  
279 sub volumes (40 mm cubes) are more representative of the scale and hence the macropore  
280 distribution of the oedometer samples (20 mm thick) than the triaxial samples (80 mm thick).  
281 Munkholm *et al.* (2012) showed similar results for scans of agricultural soils, in that the strongest  
282 correlations were found between parameters assessed at similar levels of observation. Visual  
283 inspection of the samples (e.g. Figure 3) showed that the macropores extended through lengths  
284 equivalent to the oedometer samples but not throughout the full height of the triaxial samples.

## 285 4. Conclusions

286 XCT was used to visualise and quantify the pore structure within 100 mm diameter clay fill samples  
287 at a resolution that enabled the measurement of macropores ( $> 63 \times 10^{-6} \text{ m}$ ). The samples were  
288 scanned in both partially saturated and fully saturated conditions to investigate the evolution of the  
289 internal macropore structure following saturation. Additionally, XCT-derived pore property metrics  
290 were compared to saturated hydraulic conductivity measurements to assess the influence of  
291 macroporosity on water flow. The following conclusions can be drawn:

292 1) The XCT results show that the distribution of macropores ( $> 63 \times 10^{-6} \text{ m}$ ) was variable throughout  
293 the embankment core (between 1.5 m and 6.5 m depth). The saturated hydraulic conductivity ( $K_{sat}$ )



294 of the samples also varied throughout the embankment core, showing no clear relationship with  
295 depth. Comparative macropore data from other clay fill embankments is not available, but this result  
296 is representative of the variable, poorly compacted nature of the dumped clay fill (Vaughan *et al.*,  
297 2004; Briggs *et al.*, 2017). This is in contrast to the relationship of decreasing  $K_{sat}$  with depth  
298 measured in overconsolidated clay cuttings (Chandler, 1974; Dixon *et al.*, 2018).

299 2) The macropore length had a greater influence on the saturated hydraulic conductivity ( $K_{sat}$ ) than  
300 the total porosity within the laboratory-scale samples. This relationship was more evident for the  
301 oedometer samples with a short ( $20 \times 10^{-3}$  m) flow path than for the triaxial samples with a longer  
302 ( $80 \times 10^{-3}$  m) flow path. The macropores increased the permeability of the samples, but they were  
303 connected over relatively short lengths (the mean macropore length was up to  $1.6 \times 10^{-3}$  m).  
304 Therefore the assumption of matrix-dominated flow used in simulations of embankment hydrology  
305 (Kovacevic *et al.*, 2001; Scott *et al.*, 2007; O'Brien, 2013, Briggs *et al.*, 2016) is likely to be  
306 representative of the clay fill in the embankment core at Laverton. However, it may not be  
307 representative of embankments formed with lenses of alternative materials (e.g. a widened or  
308 repaired embankment), or representative of clay fill soil near the surface (<1.5 m depth), where  
309 visible cracks and fissures can develop over greater lengths (Dixon *et al.*, 2018).

310 3) The process of saturation and laboratory testing altered the macropore structure of the clay fill  
311 samples. The largest macropores within the samples were most affected by the saturation  
312 procedure and were more sensitive to disturbance and small stress changes than the smaller pores.  
313 This is in agreement with measurements taken during the compaction of sediments (Delage &  
314 Lefebvre, 1984) and the consolidation of residual clay (Pender *et al.*, 2009). Therefore the  
315 contribution of macropores to water flow within clay fill soils at low effective stress (e.g. within a  
316 small embankment) may not be captured during laboratory testing; leading to underestimates of the  
317 *in situ* water flow and storage characteristics (e.g. permeability, porosity).

## 318 5. Acknowledgements

319 The authors are grateful to the University of Bath Alumni Fund and the EPSRC-funded iSmart project  
320 partners (EP/K027050/1). Thank you to D. Fairley and R. Brislin for access to the GWR and to D.  
321 Gunn, J. Chambers, B. Dashwood and S. Donohue for providing the soil samples and information.  
322 Thank you to the University of Bath technical support staff including D. Williams, D. Surgenor and C.  
323 Ball.

324

## 325 6. References

- 326 Ambrose, J. (1973) Computerized Transverse Axial Scanning (Tomography): Part 2: Clinical  
327 Application', *British Journal of Radiology*, 46, p. 1023
- 328 Anderson, S.H., Udawatta, R.P., Kumar, S., Gantzer, C.J., Rachman, A., Gilkes, R.J., Gilkes, R. and  
329 Prakougek, N. (2010). CT-measured macropore parameters for estimating saturated hydraulic  
330 conductivity at four study sites. In *19th World Congress of Soil Science, Soil Solutions for a Changing*  
331 *World, Brisbane, Australia*, pp. 13-16.
- 332 Beven, K. and Germann, P. (2013) Macropores and water flow in soils revisited, *Water Resources*  
333 *Research*, 49(6), pp. 3071–3092. doi: 10.1002/wrcr.20156.
- 334 Briggs, K.M, Smethurst, J.A., Powrie, W. and O'Brien, A.S. (2016). The influence of tree root water  
335 uptake on the long term hydrology of a clay fill railway embankment. *Transportation Geotechnics*, 9,  
336 31–48.
- 337 Briggs, K.M., Loveridge, F. A. and Glendinning, S. (2017) Failures in transport infrastructure  
338 embankments, *Engineering Geology*. Elsevier B.V., 219, pp. 107–117. doi:  
339 10.1016/j.enggeo.2016.07.016.
- 340 British Standards Institution (1990). 1377–2: *Methods of test for soils for civil engineering*  
341 *purposes—Part 2: classification tests*.
- 342 British Standards Institution (1990). 1377–5: *Methods of test for soils for civil engineering*  
343 *purposes—Part 5: Compressibility, permeability and durability tests*.
- 344 Chandler, R.J. (1974). Lias clay: the long-term stability of cutting slopes. *Géotechnique*, 24(1), pp.21-  
345 38.
- 346 Clayton, C.R.I. and Siddique, A. (1999). Tube sampling disturbance—forgotten truths and new  
347 perspectives. *Proceedings of the Institution of Civil Engineers-Geotechnical Engineering*, 137(3),  
348 pp.127-135.
- 349 Clothier, B.E., Green, S.R. and Deurer, M. (2008). Preferential flow and transport in soil: progress and  
350 prognosis. *European Journal of Soil Science*, 59(1), pp.2-13.
- 351 Cnudde, V. and Boone, M.N. (2013) High-resolution X-ray computed tomography in geosciences: A  
352 review of the current technology and applications, *Earth-Science Reviews*. Elsevier B.V., 123, pp. 1–  
353 17. doi: 10.1016/j.earscirev.2013.04.003.
- 354 Darcy, H. (1856). *Les fontaines publiques de la ville de Dijon* Dalmont, Paris.
- 355 Delage, P. and Lefebvre, G. (1984). Study of the structure of a sensitive Champlain clay and of its  
356 evolution during consolidation. *Canadian Geotechnical Journal*, 21(1), pp.21-35.
- 357 Diamond, S. (1970) Pore Size Distributions in Clays, *Clays and Clay Minerals*, 18(1), pp. 7–23. doi:  
358 10.1346/CCMN.1970.0180103.
- 359 Dixon, N., Crosby, C.J., Stirling, R., Hughes, P.N., Smethurst, J., Briggs, K., Hughes, D., Gunn, D.,  
360 Hobbs, P., Loveridge, F.A., Glendinning, S., Dijkstra, T. and Hudson, A. (2018). In situ measurements  
361 of near-surface hydraulic conductivity in engineered clay slopes. *Quarterly Journal of Engineering*  
362 *Geology and Hydrogeology*.

363 Dyer, M., Utili, S. and Zielinski, M. (2009). Field survey of desiccation fissuring of flood  
364 embankments. In *Proceedings of the Institution of Civil Engineers-Water Management*, Vol. 162, No.  
365 3, pp. 221-232. Thomas Telford Ltd.

366 Eck, D.V., Qin, M., Hirmas, D.R., Giménez, D. and Brunzell, N.A. (2016). Relating quantitative soil  
367 structure metrics to saturated hydraulic conductivity. *Vadose Zone Journal*, 15(1).

368 Geistlinger, H. (2013) Mass transfer processes across the Capillary Fringe: Quantification of gas-  
369 water interface and bubble mediated mass transfer, *EGU General Assembly*, Vienna 15(i), p. 3343

370 Glendinning, S., Hughes, P., Helm, P., Chambers, J., Mendes, J., Gunn, D., Wilkinson, P. and  
371 Uhlemann, S. (2014). Construction, management and maintenance of embankments used for road  
372 and rail infrastructure: implications of weather induced pore water pressures. *Acta Geotechnica*,  
373 9(5), pp.799-816.

374 Gunn, D., Dashwood, B.A., Bergamo, P. and Donohue, S. (2016). Aged embankment imaging and  
375 assessment using surface waves. *Proceedings of the Institution of Civil Engineers-Forensic*  
376 *Engineering*, 169(4), pp.149-165.

377 Hounsfeld, G. (1973) Computerized transverse axial scanning (tomography): part 1. Description of  
378 system, *British Journal of Radiology*, 46, pp. 1016–1022.

379 Iassonov, P., Gebrenegus, T. and Tuller, M. (2009). Segmentation of X-ray computed tomography  
380 images of porous materials: A crucial step for characterization and quantitative analysis of pore  
381 structures. *Water Resources Research*, 45(9).

382 Ito, M. and Azam, S. (2017). Determination of water flow through clayey slurries using computed  
383 micro-tomography. *Quarterly Journal of Engineering Geology and Hydrogeology*, 51(1), pp.49-62.

384 Jang, J., Narsilio, G.A. and Santamarina, J.C. (2011) Hydraulic conductivity in spatially varying  
385 media—a pore-scale investigation, *Geophysical Journal International*, Volume 184, Issue 3, 1 March  
386 2011, Pages 1167–1179, <https://doi.org/10.1111/j.1365-246X.2010.04893.x>

387 Jarvis, N.J. (2007). A review of non-equilibrium water flow and solute transport in soil macropores:  
388 Principles, controlling factors and consequences for water quality. *European Journal of Soil Science*,  
389 58(3), pp.523-546.

390 Jarvis, N., Koestel, J. and Larsbo, M. (2016). Understanding preferential flow in the vadose zone:  
391 Recent advances and future prospects. *Vadose Zone Journal*, 15(12).

392 Katuwal, S., Moldrup, P., Lamandé, M., Tuller, M. and De Jonge, L.W. (2015). Effects of CT number  
393 derived matrix density on preferential flow and transport in a macroporous agricultural soil. *Vadose*  
394 *Zone Journal*, 14(7).

395 Kovacevic, N., Potts, D.M. and Vaughan, P.R. (2001). Progressive Failure in Clay Embankments Due to  
396 Seasonal Climate Changes. *Proceedings of the International Conference on Soil Mechanics and*  
397 *Geotechnical Engineering* Vol. 3. AA Balkema Publishers, pp. 2127–2130.

398 Lamorski, K., Slawinski, C. and Barna, G. (2014) Estimation of water saturated permeability of soils,  
399 using 3D soil tomographic images and pore-level transport phenomena modelling, *EGU General*  
400 *Assembly 2014, Vienna, Austria*, (Vol. 16), p. 11775

401 Larsbo, M., Koestel, J. and Jarvis, N. (2014) Relations between macropore network characteristics  
402 and the degree of preferential solute transport, *Hydrology and Earth System Sciences*, 18(12), pp.  
403 5255–5269. doi: 10.5194/hess-18-5255-2014.

404 Li L.J.H., Zhang L and Kwong B.C.P. (2011) Field permeability at shallow depth in a compacted fill.  
405 *Proceedings of the Institution of Civil Engineers – Geotechnical Engineering* 164(3): 211–221.

406 Luo, L., Lin, H. and Halleck, P. (2008) Quantifying Soil Structure and Preferential Flow in Intact Soil  
407 Using X-ray Computed Tomography, *Soil Science Society of America Journal*, 72(4), pp. 1058–1069

408 Luo, L., Lin, H. and Li, S. (2010) Quantification of 3-D soil macropore networks in different soil types  
409 and land uses using computed tomography, *Journal of Hydrology*. Elsevier B.V., 393(1–2), pp. 53–64.  
410 doi: 10.1016/j.jhydrol.2010.03.031.

411 Mees, F., Swennen, R., Van Geet, M. and Jacobs, P. (2003). Applications of X-ray computed  
412 tomography in the geosciences. *Geological Society, London, Special Publications*, 215(1), pp.1-6.  
413 Nikon (2019). *Insight into the inside. Industrial X-ray and CT*. Nikon Metrology Europe NV. Belgium.

414 Mooney, S. (2002) Three-dimensional visualization and quantification of soil macroporosity and  
415 water flow patterns using computed tomography, *Soil Use and Management*, 18(2), pp. 142–151.  
416 doi: 10.1079/SUM2002121

417 Mooney, S., Pridmore, T., Helliwell, J. & Bennett, M. (2012) Developing X-ray computed tomography  
418 to non-invasively image 3-D root systems architecture in soil, *Plant and Soil*, 352, pp. 1–22.

419 Muddle, D.E. (2017). *The effects of soil macroporosity on the hydrology of infrastructure slopes*.  
420 Thesis (Ph.D.) - University of Bath, 2017.

421 Munkholm, L.J., Heck, R.J. and Deen, B. (2012) ‘Soil pore characteristics assessed from X-ray micro-  
422 CT derived images and correlations to soil friability’, *Geoderma*, 181–182, pp. 22–29. doi:  
423 10.1016/j.geoderma.2012.02.024.

424 Naveed, M., Moldrup, P., Arthur, E., Wildenschild, D., Eden, M., Lamandé, M., Vogel, H.J. and De  
425 Jonge, L.W. (2013). Revealing soil structure and functional macroporosity along a clay gradient using  
426 X-ray computed tomography. *Soil Science Society of America Journal*, 77(2), pp.403-411.

427 O'Brien, A.S., Ellis, E.A. and Russell, D. (2004). Old railway embankment clay fill–laboratory  
428 experiments, numerical modelling and field behaviour. In *Advances in geotechnical engineering: The*  
429 *Skempton Conference*. Thomas Telford, London, pp. 911-921.

430 O'Brien, A.S. (2013). The assessment of old railway embankments – time for a change? *Partial*  
431 *Saturation in Compacted Soils: Géotechnique Symposium in Print 2011*, pp. 19–32  
432 (<http://dx.doi.org/10.1680/geot.sip11.ks>)

433 Ommaya, A.K., Murray, G., Ambrose, J., Richardson, A. and Hounsfield, G. (1976). Computerized axial  
434 tomography: estimation of spatial and density resolution capability. *The British Journal of Radiology*,  
435 49(583), pp.604-611.

436 Pender, M.J., Kikkawa, N. and Liu, P. (2009). Macro-void structure and permeability of Auckland  
437 residual clay. *Geotechnique*, 59(9), pp.773-778.

438 Perret, J., Prasher, S.O., Kantzas, A. and Langford, C. (1999). Three-dimensional quantification of  
439 macropore networks in undisturbed soil cores. *Soil Science Society of America Journal*, 63(6),  
440 pp.1530-1543.

441 Peth, S., Nellesen, J., Fisher, G., Beckman, F. and Horn, R. (2010). Dynamics of soil pore space  
442 structure investigated by X-ray microtomography. In *19th World Congress of Soil Science, Soil*  
443 *Solutions for a Changing World, Brisbane, Australia*, pp.17-20.

444 Powrie, W. (2014). Soil mechanics: concepts and applications. *CRC Press*. London.

445 Rowe, P.W. (1972). The relevance of soil fabric to site investigation practice. *Geotechnique*, 22(2),  
446 pp.195-300.

447 Scott, J.M., Loveridge, F. and O'Brien, A.S. (2007). Influence of climate and vegetation on railway  
448 embankments. In: Cue'llar, V., Dapena, E., Alonso, E., *et al.* (Eds.), *Proceedings of the 14th European*  
449 *Conference on Soil Mechanics and Geotechnical Engineering, Madrid*. Millpress, Amsterdam, the  
450 Netherlands, pp. 659–664.

451 Schindelin, J., Arganda-Carreras, I., Frise, E., Kaynig, V., Longair, M., Pietzsch, T., Preibisch, S.,  
452 Rueden, C., Saalfeld, S., Schmid, B. and Tinevez, J.Y.(2012) 'Fiji - an Open Source platform for  
453 biological image analysis', *Nature methods*, 9(7), p. 10.1038/nmeth.2019. doi: 10.1038/nmeth.2019.

454 Shin, H. S., Kim, K. Y. and Pande, G. N. (2013) 'Porosity and Pore-Size Distribution of Geomaterials  
455 from X-ray CT Scans', in Laloui, L. and Ferrari, A. (eds) *Multiphysical Testing of Soils and Shales SE -*  
456 *21*. Springer Berlin Heidelberg (Springer Series in Geomechanics and Geoengineering), pp. 177–186.  
457 doi: 10.1007/978-3-642-32492-5\_21.

458 Smith, J. C. (2015) Examining Soil Based Construction Materials through X-Ray Computed  
459 Tomography. Thesis (Ph.D.) Durham University.

460 Spearman, C. (1904). The proof and measurement of association between two things. *The American*  
461 *Journal of Psychology*, 15(1), pp.72-101.

462 Taina, I.A., Heck, R.J. & Elliot, T.R. (2008) 'Application of X-ray computed tomography to soil science:  
463 a literature review', *Canadian Journal of Soil Science*, 88, pp. 1–19.

464 Terzaghi, K. (1943). Theory of consolidation. *Theoretical Soil Mechanics*, pp.265-296.

465 Vaughan, P.R., Kovacevic, N., Potts, D.M. (2004). Then and now: some comments on the design and  
466 analysis of slopes and embankments. Advances in Geotechnical Engineering. *The Skempton*  
467 *Conference*. Thomas Telford, London, pp. 241–290.

468 Wildenschild, D. and Sheppard, A.P. (2013) 'X-ray imaging and analysis techniques for quantifying  
469 pore-scale structure and processes in subsurface porous medium systems', *Advances in Water*  
470 *Resources*. Elsevier Ltd, 51, pp. 217–246. doi: 10.1016/j.advwatres.2012.07.018.

471 Washburn, E.W. (1921).The dynamics of capillary flow. *Physical Review*, 17(3), p.374

472

473 **7. Tables**

474 *Table 1: The labels and details of the samples excavated from Laverton Embankment (both in situ*  
475 *and saturated conditions shown)*

476 *Table 2: The XCT scanner settings used to scan samples from Laverton Embankment*

477 *Table 3: The voxel resolution achieved from XCT scan of the 100 mm diameter clay fill core samples*  
478 *from Laverton Embankment. The greyscale threshold values (256 levels) are shown in brackets.*

479 *Table 4: The pore property metrics for 40 mm cubed (central) sub volumes of clay fill calculated using*  
480 *XCT image data*

481 *Table 5: Mercury Intrusion Porosimetry (MiP) results and total porosity for Sample 5C<sub>(bot)</sub> and the*  
482 *Reconstituted Sample.*

483 *Table 6: Porosity and saturated hydraulic conductivity measurements from triaxial permeability tests*  
484 *and one-dimensional consolidation tests on the saturated clay fill samples*

485

## 486 8. Figures

487

488 *Figure 1: Laverton Embankment in Gloucestershire as viewed (a) from the road, (b) from above.*

489 *Figure 2: A profile showing the volume of voids throughout the height of Sample 5C. This profile is*  
490 *composed of data from three individual sub volumes (40 mm sub volumes) at the top, the middle and*  
491 *the bottom of the sample*

492 *Figure 3: Three dimensional visualisations of macropore structure within 40 mm sub volumes of (a)*  
493 *Initial Sample 5C<sub>(bot)</sub>, (b) Saturated Sample 5C<sub>(bot)</sub>, (c) The Reconstituted Sample. These samples had*  
494 *a corrected macroporosity of 58%, 53% and 40% respectively (Table 4).*

495 *Figure 4: Profiles showing the volume of voids per slice for each of the samples, located between 1.5-*  
496 *6.5 m below the embankment surface.*

497 *Figure 5: Profiles showing the volume of voids within per slice (%) from the XCT data before and after*  
498 *sample saturation for samples (a) 2C, (b) 3C and (c) 4C.*

499 *Figure 6: Spearman's correlation coefficients for the pore property metrics from the saturated clay*  
500 *fills samples and the laboratory hydraulic conductivity measurements.*

501 *Figure 7: A flowchart outlining the key stages of the XCT image analysis procedure.*

502 *Figure 8: A midsection slice from the reconstituted sample image data (40 mm cube sub volume)*  
503 *subjected to (a) no filter, (b) a median filter, (C) a sharpened median filter, (d) a non-local means*  
504 *filter, and (e) a Gaussian filter.*

505 *Figure 9: Greyscale intensity histograms for the reconstituted sample after the application of image*  
506 *enhancement techniques (shown in images).*

507 *Figure 10: A midsection slice through the reconstituted sample (40 mm cube sub volume) (a) prior to*  
508 *segmentation, (b) after thresholding using the fully automated watershed method, (c) after manual*  
509 *thresholding using the interactive method. The pores are shown as black. The segmented pores are*  
510 *shown as blue.*

511 *Figure 11: The impact of partial volume correction (2 voxels) on pore volume throughout the*  
512 *reconstituted sample.*

513

## 514 9. Appendix

515 An initial investigation was used to develop the image analysis procedure for the clay fill samples  
516 (Muddle, 2017) by first examining a reconstituted clay fill sample (100 mm diameter, 87 mm height).  
517 A flowchart outlining the key stages of the XCT image analysis procedure is shown in Figure 7. The  
518 details of the filtering, thresholding and partial volume correction stages are described below.

519 Figure 8 shows images of the midsection slice from a 40 mm sub volume of the reconstituted clay fill  
520 sample with different applied filters. All of the filters reduced the level of noise present within the  
521 images. The sharpened median filter and the non-local mean filter gave the sharpest contrast  
522 between phases with the most defined pore edges. The Gaussian filter and the median filter showed  
523 blurring of the pore boundaries. Examination of the greyscale intensity histograms (Figure 9) shows  
524 that the median and Gaussian filters did not significantly improve the definition of the material  
525 phase peaks within the greyscale histograms. The sharpened median filter and the non-local means  
526 filter improved the image quality and the definition of peaks. The sharpened median filter was twice  
527 as computationally efficient as the non-local means filter and was therefore selected for the  
528 subsequent analyses.

529 The effectiveness of automated watershed thresholding in relation to interactive manual  
530 thresholding was compared by visual assessment of slices throughout the height of the  
531 reconstituted clay fill sample. Figure 10a shows an image with a sharpened median filter prior to  
532 segmentation. This can be compared with the same slice after the application of automated  
533 watershed thresholding (Figure 10b) and the manual method (Figure 10c). These Figures show that  
534 the automated thresholding method produced more unsegmented pores than the manual method.  
535 The manual method was a more reliable segmentation method than the automated method for a  
536 sample of clay fill with intensity histograms lacking complete definition.

537 All objects with an equivalent diameter less than two voxels ( $106\text{-}126 \times 10^{-6}$  m) were removed from  
538 the image data prior to quantification of the macropore property metrics. The partial volume  
539 correction removed a large number of objects from the images for the reconstituted sample. This is  
540 because the reconstituted sample had a relatively uniform pore size and distribution, with few large  
541 macropores compared to the number of smaller macropores. While a large number of pores were  
542 removed, particularly in the largest sub volume, the volume of removed pores was small. The effect  
543 of a two voxel partial effect correction on the total calculated macroporosity was between 0.02 %  
544 and 0.04 % of sample volume depending on the size of the subsample.

545 Figure 11 shows the influence of the partial volume correction on the profile of volume of pores per  
546 slice through the height of the reconstituted sample. The correction does not significantly alter the  
547 profile, with the exception of one section at the centre of the subsample with a higher  
548 macroporosity. The difference indicates that the increase in macroporosity in the middle slices was  
549 due to many individual, small macropores rather than fewer, larger macropores. The measured  
550 increase in macroporosity was a consequence of the laboratory preparation of the reconstituted  
551 sample.



## 7. Tables

*Table 1: The labels and details of the samples excavated from Laverton Embankment (both in situ and saturated conditions shown)*

	2C	2C saturated	3C	3C saturated	4C	4C saturated	5C-top	5C-top saturated	5C-mid	5C-bot	5C-bot saturated	6C	6C saturated	7C*	Reconstituted
Height ( $\times 10^{-3}$ m)	98	86	87	80	92	78	92	83	107	94	75	91	78	92	87
Diameter ( $\times 10^{-3}$ m)	102	102	102	102	102	102	102	102	102	102	102	87	87	87	100
Bulk density ( $\times 10^{-3}$ kg/m <sup>3</sup> )	1.75	1.73	1.79	1.79	1.85	1.91	1.80	1.79	1.84	1.84	1.89	1.81	1.85	1.87	1.91
Origin - depth of centre of sample from the surface (m)	1.50	1.50	2.51	2.51	3.51	3.51	4.50	4.50	4.54	4.58	4.58	5.51	5.51	6.51	3.58
Water content (gravimetric %)	25	31	26	34	26	29	26	29	26	26	30	25	33	24	33

\* Sample 7C could not be saturated and rescanned due to the fragmented nature of the sample

Table 2: The XCT scanner settings used to scan samples from Laverton Embankment

Sample	Voltage (kV)	Current (mA)	Exposure (ms)	Projections	Vertical slices	Other
102 or 87 mm diameter cylindrical sample	195	105	2000	1800	1998	Copper* filter (0.5 mm thick)

\* Copper filter used to reduce beam hardening

Table 3: The voxel resolution achieved from XCT scan of the 100mm diameter clay fill core samples from Laverton Embankment. The greyscale threshold values (256 levels) are shown in brackets.

Sample	Voxel resolution ( $\times 10^{-6}$ m)	Sample	Voxel resolution ( $\times 10^{-6}$ m)	Sample	Voxel resolution ( $\times 10^{-6}$ m)
2C (25)	58.2	5C-top* <sup>2</sup> (50)	57.3	6C (48)	53.4
2C saturated* <sup>1</sup> (26)	61.1	5C-top saturated* <sup>1</sup> (53)	61.5	6C saturated* <sup>1</sup> (53)	52.9
3C (48)	54.8	5C-mid* <sup>2</sup> (55)	53.7	7C (60)	54.4
3C saturated* <sup>1</sup> (24)	60.4	5C-bot* <sup>2</sup> (46)	54.7	Recon (105)	62.7
4C (50)	55.5	5C-bot saturated* <sup>1</sup> (49)	59.7		
4C saturated* <sup>1</sup> (58)	58.2				

\*<sup>1</sup> Saturated and unsaturated sample resolutions were matched using the PVE correction to allow for comparison between the samples.

\*<sup>2</sup> The resolution of the three samples within 5C were matched using the PVE correction to allow for porosity throughout the height of the sample to be compared.

Table 4: The pore property metrics for 40 mm cubed (central) sub volumes of clay fill calculated using XCT image data

	2C	2C saturated	3C	3C saturated	4C	4C saturated	5C-top	5C-top saturated	5C-mid	5C-bot	5C-bot saturated	6C	6C saturated	7C	Reconstituted
Corrected															
Macroporosity (%)	1.98	0.81	2.03	1.72	0.38	0.15	1.85	1.80	1.30	0.58	0.53	0.18	0.11	4.12	0.40
Macropore density ( $\times 10^6$ ) (number/m <sup>3</sup> )	66.14	57.76	60.86	35.08	89.62	13.20	142.42	83.45	149.95	74.87	56.45	29.11	25.75	59.84	51.70
Mean macropore length ( $\times 10^{-3}$ m)	1.09	0.98	1.13	0.96	1.05	1.19	1.59	1.43	1.58	1.57	1.41	0.80	0.81	2.02	0.98
Surface area density (m <sup>2</sup> /m <sup>3</sup> )	207.87	110.62	198.45	188.52	86.00	19.76	264.18	209.68	203.25	88.81	70.68	34.75	23.76	337.64	69.15
Mean volume of ten largest pores ( $\times 10^{-9}$ m <sup>3</sup> )	55.28	13.93	70.57	72.90	6.82	4.47	36.69	21.19	16.16	8.53	6.51	5.68	2.41	203.44	4.42

Table 5: Mercury Intrusion Porosimetry (MiP) results and total porosity for Sample 5C<sub>(bot)</sub> and the Reconstituted Sample.

	5C-bot sample	Reconstituted sample
Mass of sample ( $\times 10^{-3}$ kg)	0.49	1.39
Density ( $\times 10^3$ kg/m <sup>3</sup> )	1.78	1.91
Volume of sample ( $\times 10^{-9}$ m <sup>3</sup> )	275.83	730.05
Total specific volume of pores ( $\times 10^{-6}$ m <sup>3</sup> /kg)	152.34	134.73
Total pore volume ( $\times 10^{-9}$ m <sup>3</sup> )	74.62	187.72
Max pore entrance diameter ( $\times 10^{-6}$ m)	109.52	110.01
Min pore entrance diameter ( $\times 10^{-6}$ m)	0.0037	0.0037
Average pore entrance diameter ( $\times 10^{-6}$ m)	0.023	0.024
Modal pore entrance diameter ( $\times 10^{-6}$ m)	0.051	0.052
Median pore entrance diameter ( $\times 10^{-6}$ m)	0.042	0.043
MIP Porosity (%)	27	26
Total porosity (phase relationship) (%)	45	50

*Table 6: Porosity and saturated hydraulic conductivity measurements from triaxial permeability tests and one-dimensional consolidation tests on the saturated clay fill samples*

	2C saturated	3C saturated	4C saturated	5C-top saturated	5C-bot saturated	6C saturated	Reconstituted sample
Total porosity (%)	50	49	44	48	45	48	50
Oedometer (3 x 70 mm diameter, 20 mm height) - average saturated hydraulic conductivity (first loading step) ( $\times 10^{-10}$ m/s)	17.7	6.24	7.35	3.75	16.5	2.26	2.95
Triaxial (100 mm diameter, 80 mm height) - saturated hydraulic conductivity ( $\times 10^{-11}$ m/s)	10.4	5.32	16.7	80.3	10.8	1.76	8.15
Factor of difference between oedometer and triaxial measured saturated hydraulic conductivity	17.0	11.7	4.4	4.7	15.3	12.8	3.6

## 8. Figures



(a)



(b)

Figure 1: Laverton Embankment in Gloucestershire as viewed (a) from the road, (b) from above.

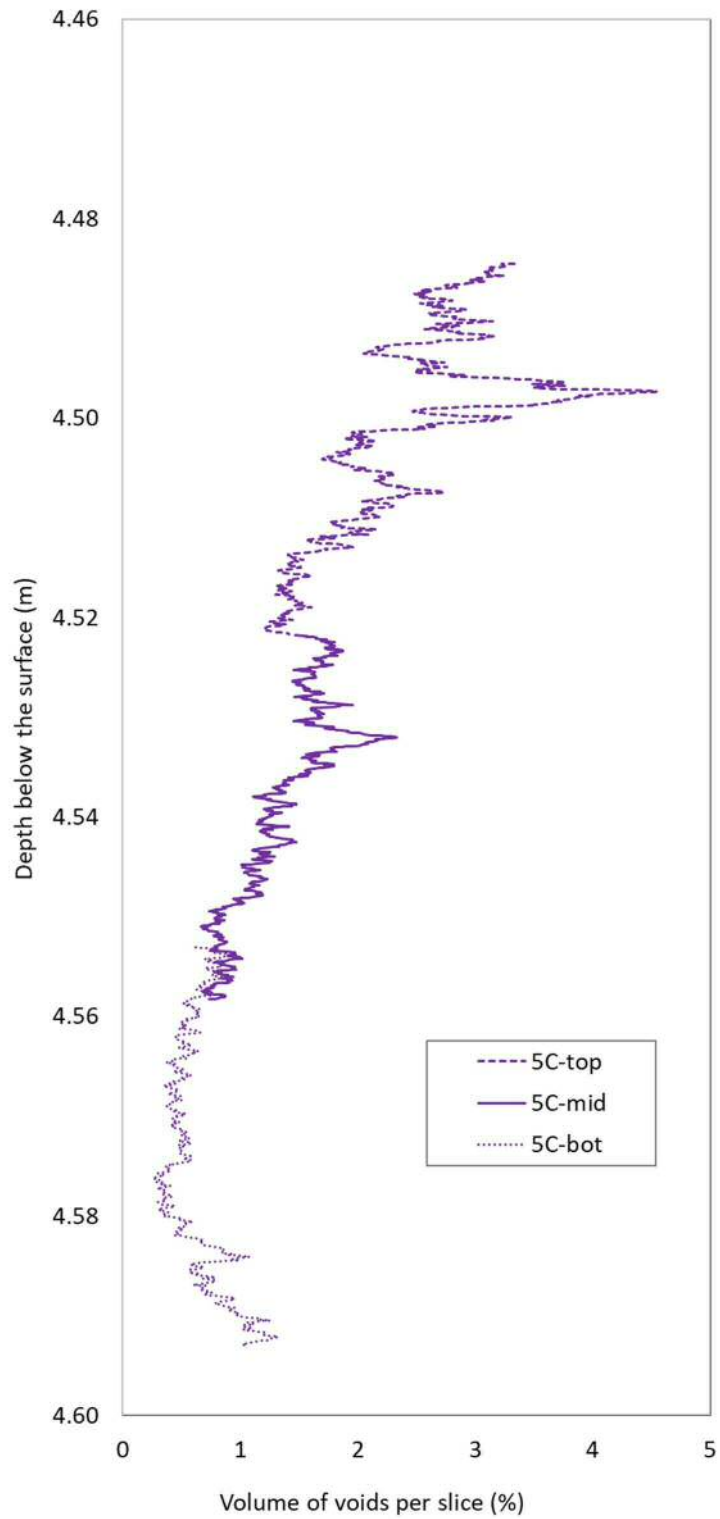
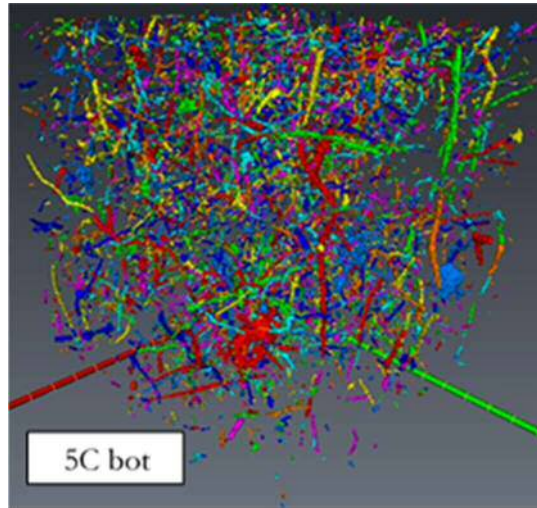
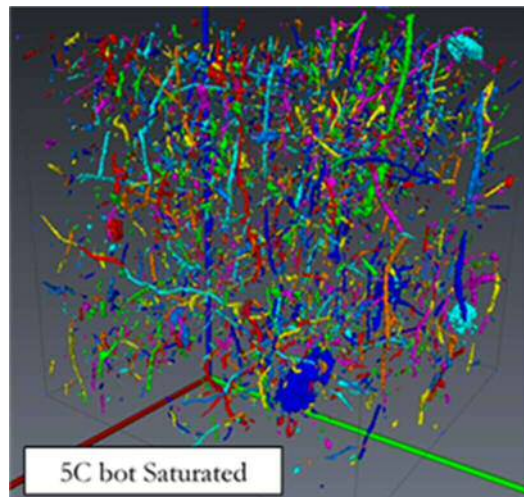


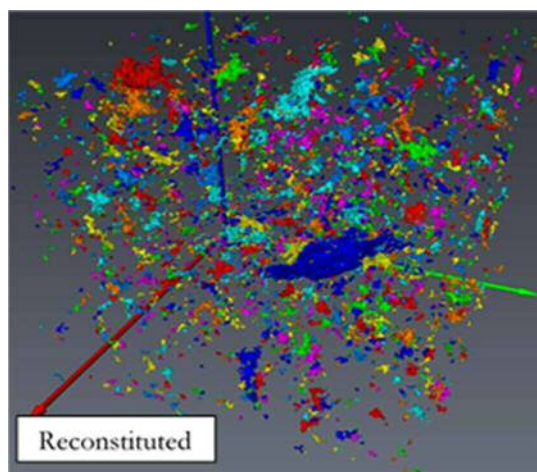
Figure 2: A profile showing the volume of voids throughout the height of Sample 5C. This profile is composed of data from three individual sub volumes (40 mm sub volumes) at the top, the middle and the bottom of the sample.



(a)



(b)



(c)

Figure 3: Three dimensional visualisations of macropore structure within 40 mm sub volumes of (a) Initial Sample  $5C_{(bot)}$ , (b) Saturated Sample  $5C_{(bot)}$ , (c) The Reconstituted Sample. These samples had a corrected macroposity of 58%, 53% and 40% respectively (Table 4).

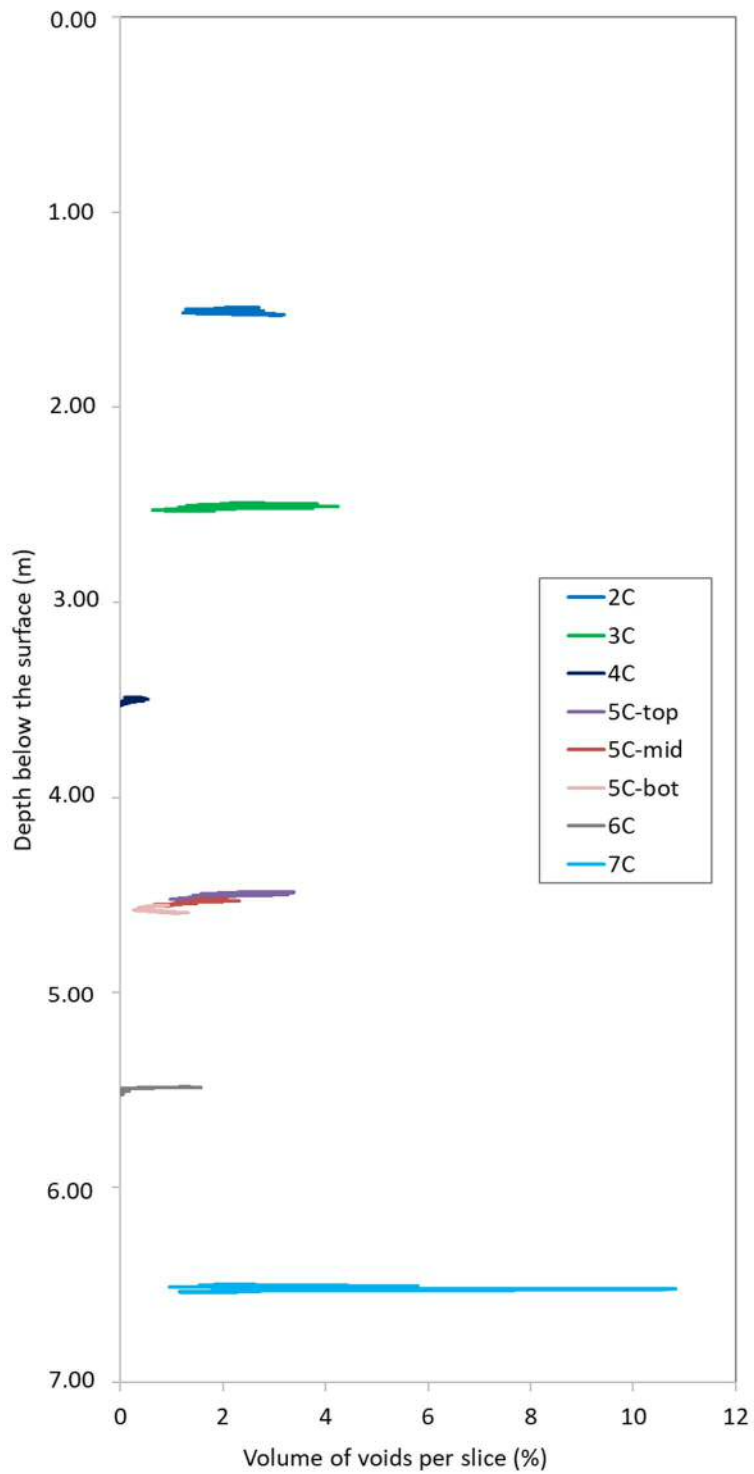
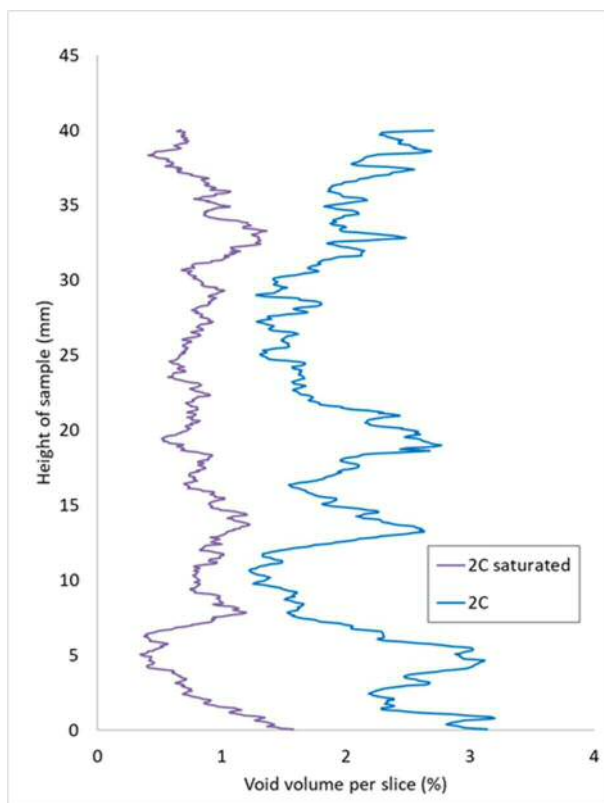
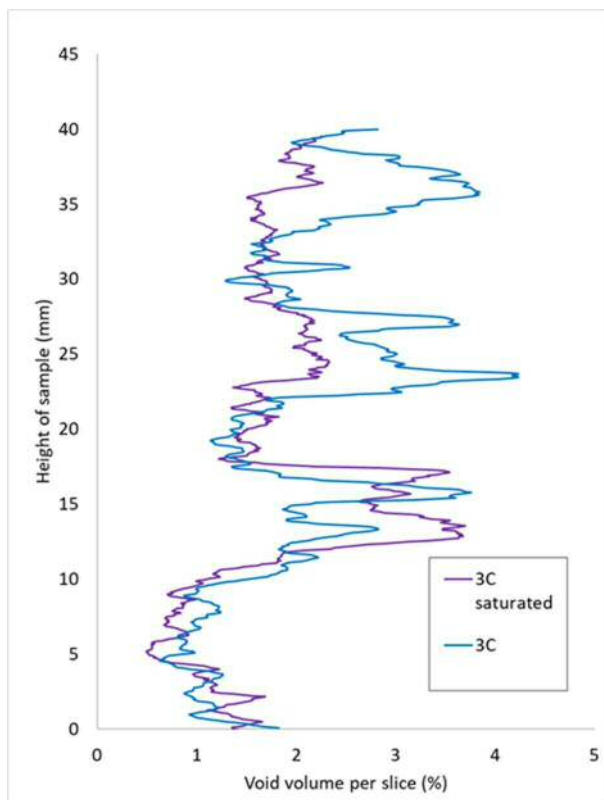


Figure 4: Profiles showing the volume of voids per slice for each of the samples, located between 1.5-6.5m depth below the embankment surface.

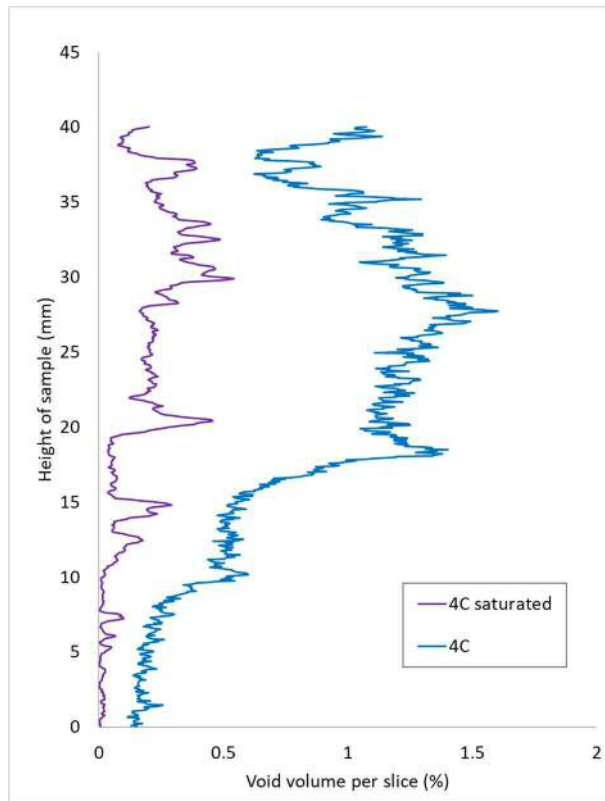




(a)



(b)



(c)

Figure 5: Profiles showing the volume of voids within per slice (%) from the XCT data before and after sample saturation for samples (a) 2C, (b) 3C and (c) 4C.

Spearman's Rho coefficients										0.8 to 1
Triaxial saturated hydraulic conductivity										0.6 to 0.8
Oedometer saturated hydraulic conductivity	<b>0.82</b>									0.4 to 0.6
Total porosity (phase relationship)	-0.45	-0.11								0.2 to 0.4
Bulk density	0.07	-0.47	-0.43							0.0
Corrected XCT-derived macroporosity	0.39	0.71	0.29	-0.65						0.0 to -0.2
Macropore density	0.43	0.75	0.38	-0.56	0.75					-0.4 to -0.6
Mean macropore length	0.96	0.86	-0.42	0.02	0.46	0.57				-0.6 to -0.8
Macropore surface area density	0.21	0.61	0.38	-0.75	0.96	0.79	0.32			-0.8 to -1
Mean volume of ten largest XCT-observed macropores	0.32	0.64	0.15	-0.65	0.93	0.5	0.36	0.86		

Figure 6: Spearman's correlation coefficients for the pore property metrics from the saturated clay fills samples and the laboratory hydraulic conductivity measurements.

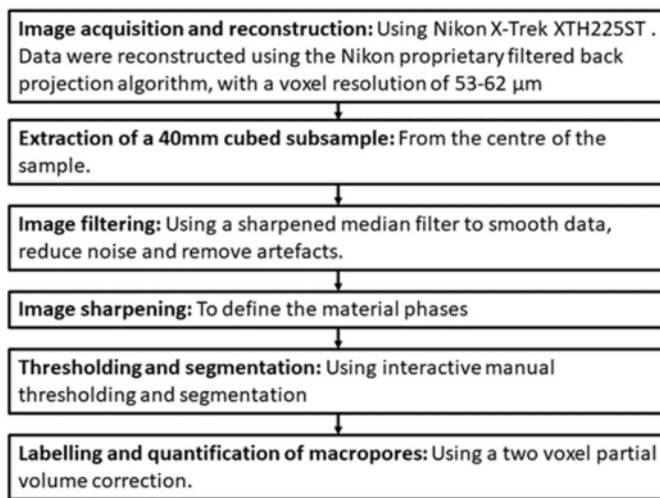
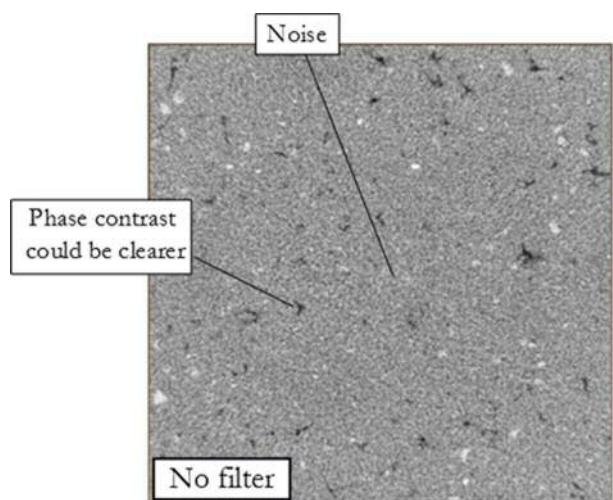
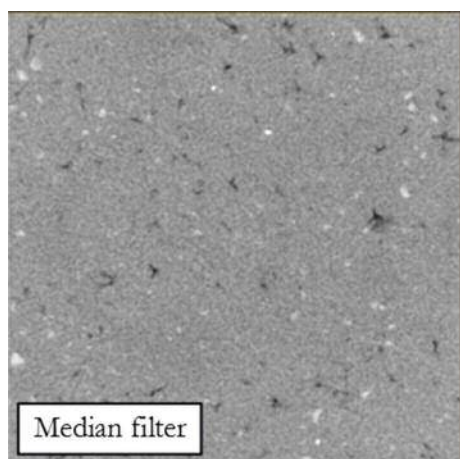


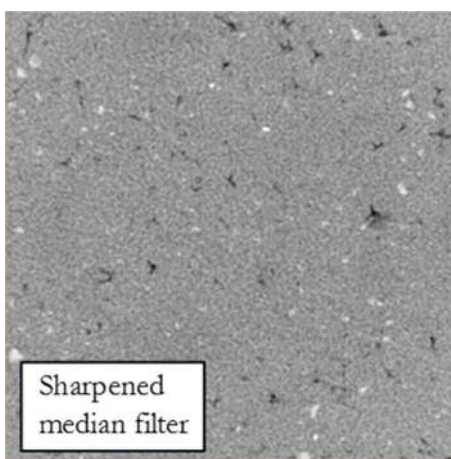
Figure 7: A flowchart outlining the key stages of the XCT image analysis procedure



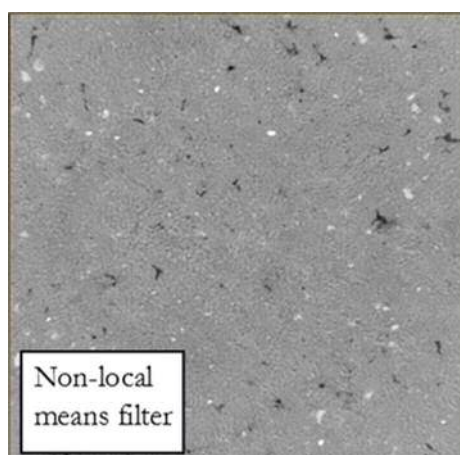
(a)



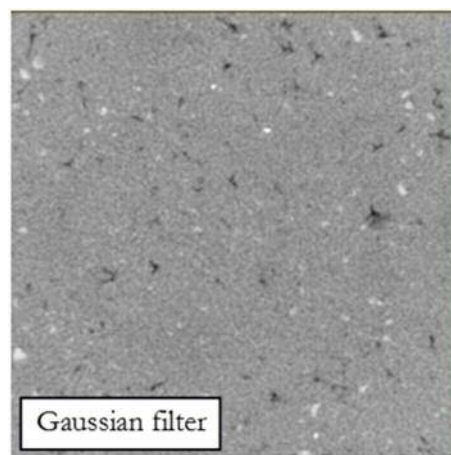
(b)



(c)



(d)



(e)

Figure 8: A midsection slice from the reconstituted sample image data (40 mm cube sub volume) subjected to (a) no filter, (b) a median filter, (c) a sharpened median filter, (d) a non-local means filter, and (e) a Gaussian filter.

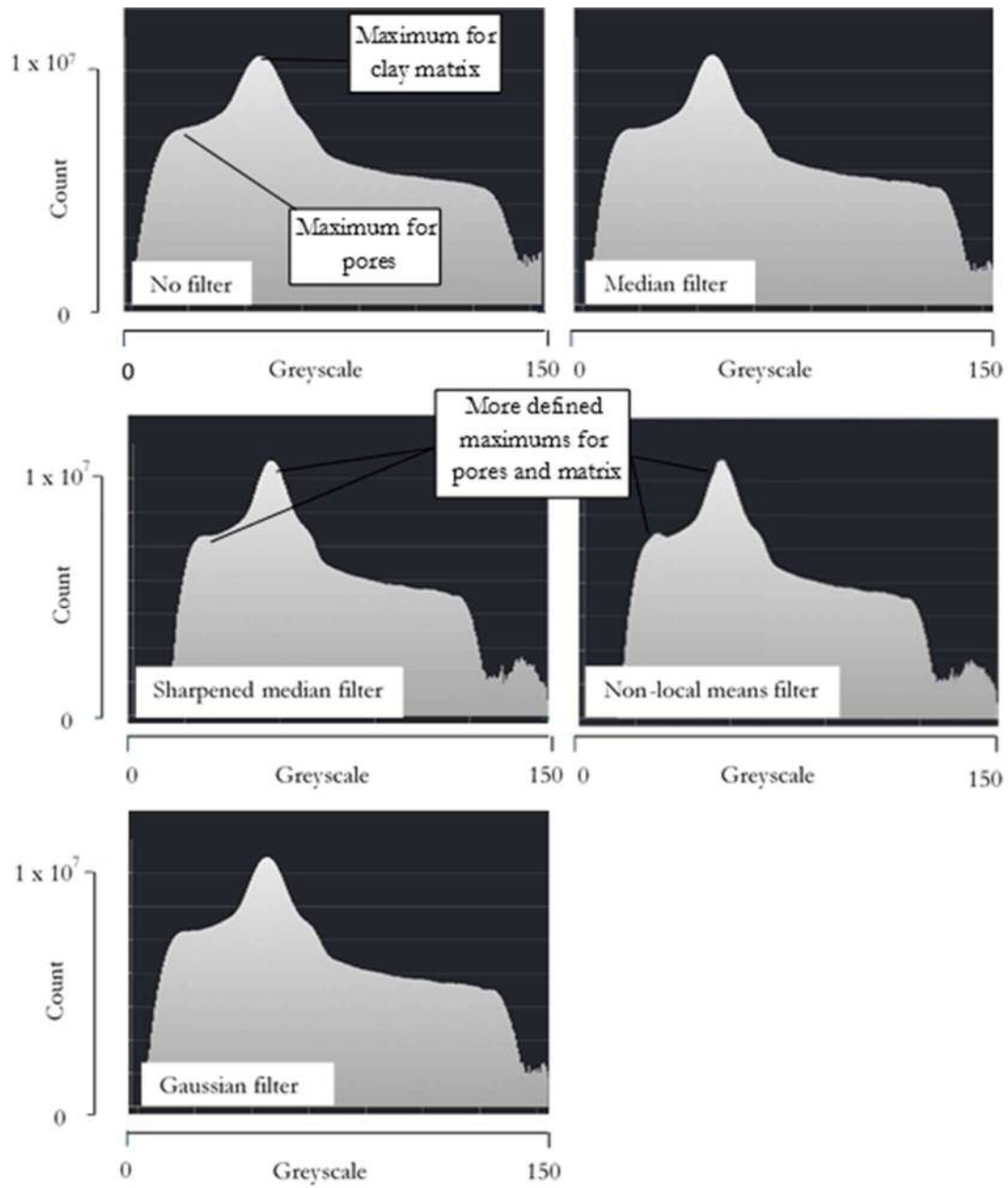
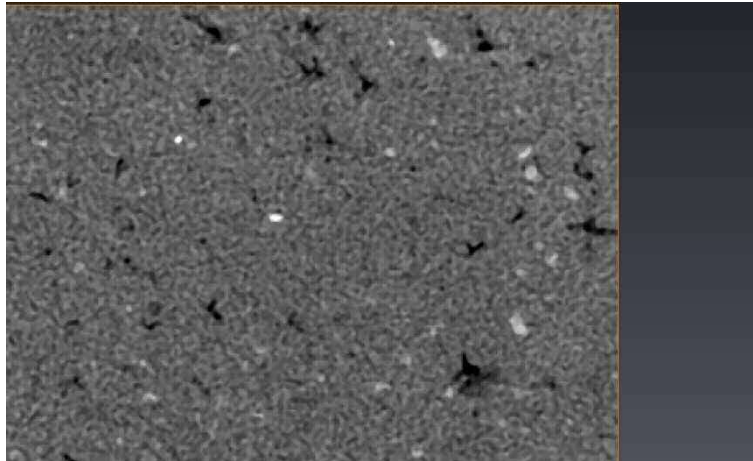
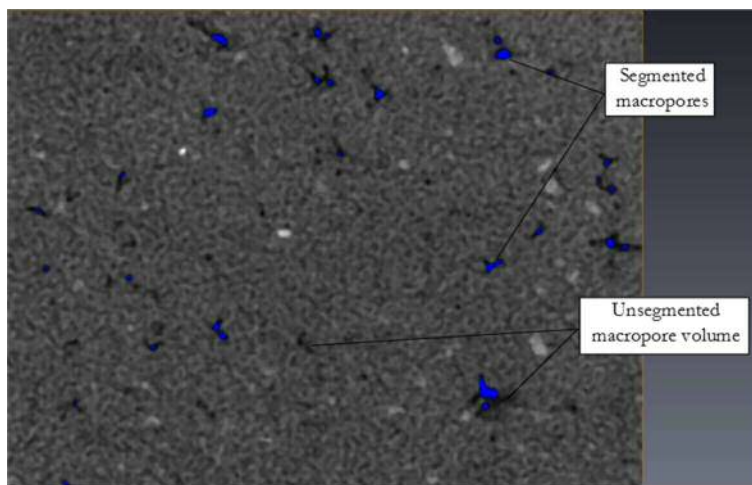


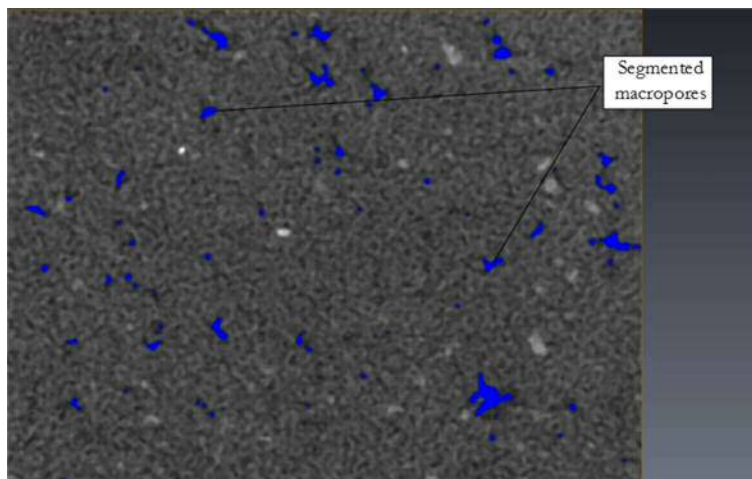
Figure 9: Greyscale intensity histograms for the reconstituted sample after the application of image enhancement techniques (shown in images).



(a)



(b)



(c)

Figure 10: A midsection slice through the reconstituted sample (40 mm cube sub volume) (a) prior to segmentation, (b) after thresholding using the fully automated watershed method, (c) after manual thresholding using the interactive method. The pores are shown as black. The segmented pores are shown as blue.

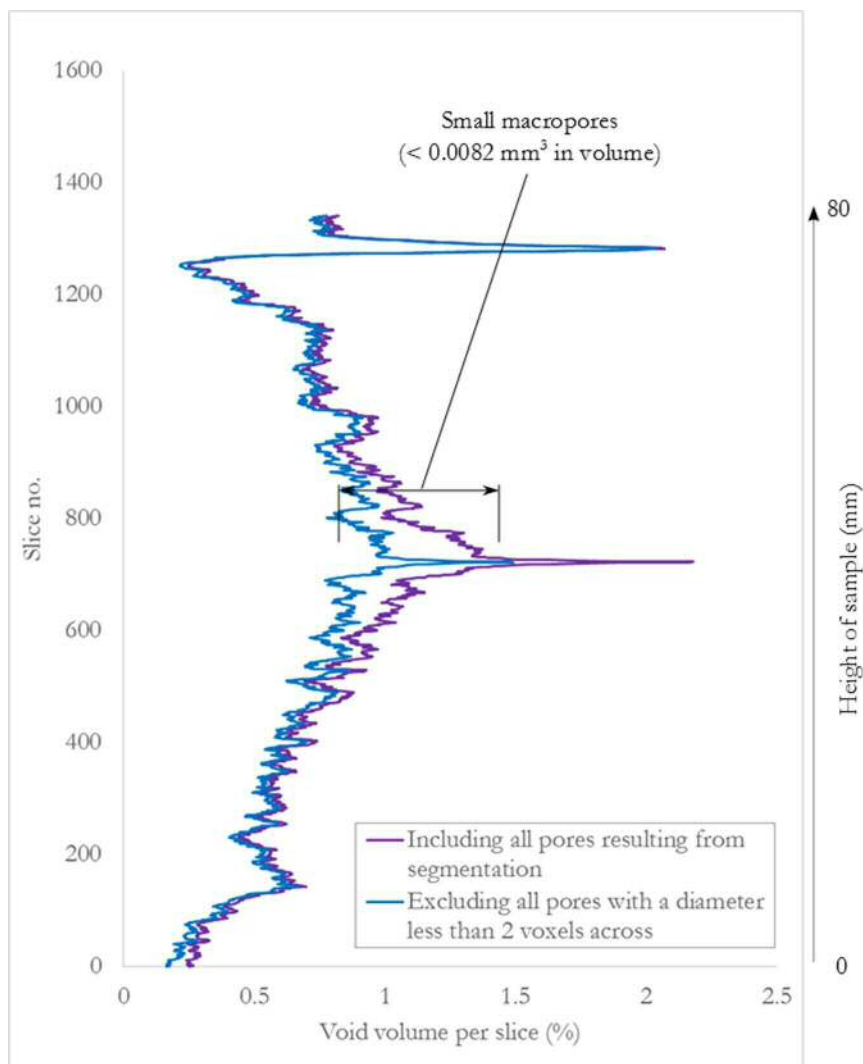


Figure 11: The impact of partial volume correction (2 voxels) on pore volume throughout the reconstituted sample.